16th World Conference on Earthquake, 16WCEE 2017
Santiago Chile, January 9th to 13th 2017
Paper N° 4899
Registration Code: S-I1464363787

EFFECT OF HIGH STRENGTH STEEL ON THE FLEXURAL BEHAVIOR OF HIGH STRENGTH CONCRETE AND FIBER-REINFORCED CONCRETE SPECIMENS

L. Ibarra[(1)] and B. Bishaw[(2)]

[(1)] *Assistant Professor, Dept. of Civil and Environmental Engineering, University of Utah, USA, luis.ibarra@utah.edu*
[(2)] *PhD Graduate, Dept. of Civil and Environmental Engineering, University of Utah, USA*

Abstract

A series of reinforced concrete (RC) components with high strength materials were tested under pure flexural monotonic and cyclic quasi-static loading protocols. The specimen materials included high strength concrete (HSC), and ultra-high strength steel (UHSS). In some specimens steel fibers were added to the concrete mix to create high strength fiber reinforced concrete (HSFRC) specimens. The series of eight specimens include, for the first time, a nonlinear response comparison of HSC and HSFRC specimens with UHSS under monotonic and cyclic loading protocols. The use of UHSS on HSC components increased the ultimate flexural capacity by more than 60%, as compared with a similar component with conventional steel and the same steel area. However, the rotational capacity of HSCfy100 specimens decreased by more than 40% due to the lower elongation at fracture of UHSS. Also, the drift at peak strength was consistently larger for monotonic tests, underlining the need of carrying out monotonic tests to identify this nonlinear parameter. The addition of steel fibers to HSC specimens increased the peak strength by an additional 10%, and greatly reduced cracking and spalling of HSC specimens. Nevertheless, the energy dissipation capacity of the specimens did not increase by the presence of fibers. The implications of different hysteretic energy dissipation capabilities were investigated using single-degree-of-freedom models subjected to far-field ground motions. For this purpose, concentrated plasticity models that account for strength and stiffness deterioration were calibrated based on the experimental results. No previous studies have simultaneously addressed the monotonic and cyclic response of HSC components with UHSS rebars. This study provides the first numerical analysis on these elements that is supported by experimental data.

Keywords: High Strength Concrete, High Strength Steel, Steel Fibers, Concentrated Plasticity.

1. INTRODUCTION

High strength materials are commonly used to reduce the size of reinforced concrete (RC) cross sections and avoid steel congestion. This study, however, focuses on the potential increase on the components' ultimate strength capacity of these elements. HSC components are implemented in non-seismic hazard zones, particularly in columns of tall buildings because HSC is more efficient in elements subjected to large axial loads. Nevertheless, HSC elements are not often used in seismic zones because they tend to exhibit early spalling that reduces the load carrying capacity, whereas the brittleness of the concrete mix reduces the ductility capacity. The ductile properties of HSC components can be enhanced by using adequate transverse reinforcement, but more stirrups lead to premature spalling, whereas concrete crushing failure is still difficult to prevent. Furthermore, the ultimate capacity of RC components controlled by flexural failure mechanisms, and relatively small axial loads, is not significantly increased by the use of HSC [1,2].

The use of high strength steel for longitudinal rebars increases the component's bending capacity, whereas its use for stirrups results in less transverse reinforcement, reducing the likelihood of early spalling. However, steel rebars with a yield strength larger than 80 ksi (551 MPa), or ultra-high strength steel (UHSS), have not been adopted in seismic regions due to concerns with their low elongation at fracture. NEHRP [3] recommends the use of UHSS only for frames located in low seismic regions, until more data is available.

Some studies have used fibers trying to reduce early spalling and cracking, and to increase the specimen's inelastic deformation capacity. Steel fibers increase the energy absorbing capability, ductility, and toughness of plain concrete [4]. Also, steel fibers may increase the ultimate load of beam-columns by more than 50%, and the concrete cracking load by more than 100% because of the crack arresting mechanism provided by the fibers [5,6]. Most of the studies on fiber reinforced concrete, however, used normal strength concrete (NSC), for instance. Tavallali et al. [7] investigated the cyclic behavior of NSC beams that include HSS, and in some cases steel fibers, reporting lower spread of plasticity. In one of the few studies on high strength fiber reinforced concrete (HSFRC) components, Daniel and Loukili [8] investigated the influence of longitudinal steel and steel fibers on HSC beams. They found that fibers increased the beams' energy dissipation for lower reinforcement ratios, but the normalized deflection at failure was smaller for HSFRC beams. Also, Ashour and Wafa [9] tested eight HSC and HSFRC beams with concrete compressive strength of 12.8 ksi (88 MPa) under two-point flexural monotonic loading. They concluded that steel fibers reduce crack propagation, and increase ductility and plastic hinge length.

Because experimental tests on RC components with high strength materials are very limited, numerical studies on the seismic performance of HSC and HSFRC buildings often extrapolate nonlinear parameters, or do not incorporate deteriorating characteristics [2,6,10]. This paper presents the results of a series of flexural tests on HSC beam-column elements, in which HSS and steel fibers were progressively added to the components. Five specimens were tested under cyclic loading, and three specimens were subjected to monotonic loading to separate the effects of strength deterioration caused by large displacements from cyclic deterioration. The implications of different hysteretic energy dissipation capabilities were investigated using single-degree-of-freedom (SDOF) models subjected to far-field ground motions. For this purpose, concentrated plasticity models that account for strength and stiffness deterioration were calibrated based on the experimental results. These numerical simulations address the monotonic and cyclic response of HSC components with UHSS rebars, and use incremental dynamic analyses to assess the effect of high strength materials on the response of SDOF systems.

2. EXPERIMENTAL INVESTIGATION

2.1. Experimental Setup

Experimental tests were performed on HSC components, in which UHSS and steel fibers were sequentially incorporated. The specimen matrix included monotonic and cyclic loading protocols to separate the effects of strength deterioration due to large displacements from cyclic deterioration caused by cumulative damage. Eight

specimens with a cross section of 254 × 254 mm (10 × 10 in.), and a total length of 2,134 mm (84 in.) where subjected to monotonic and cyclic loads. The specimens included a central stub of a width of 203 mm (8 in.), where loads were vertically applied (Fig. 1a). The unbraced length from the face of the stub to the end support, or shear span, was a = 813 mm (32 in.). The specimens were simply supported on semi-circular plates made of half HSS 114 x 13 mm (4.5 x 0.5 in.) to allow ends to rotate. On the north side end, angles at the sides of the semi-circular plates prevented translation, creating a pinned boundary condition. The south end of the beams simulated a roller boundary condition.

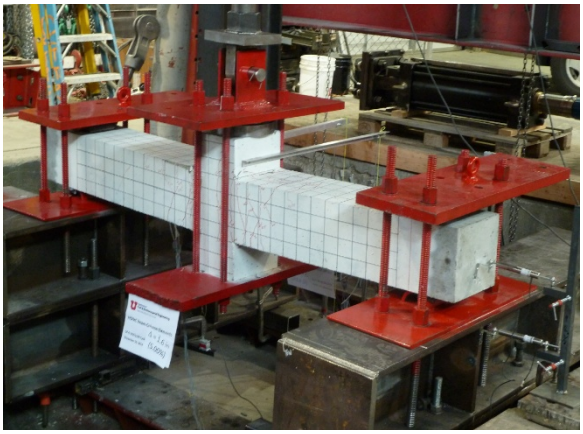

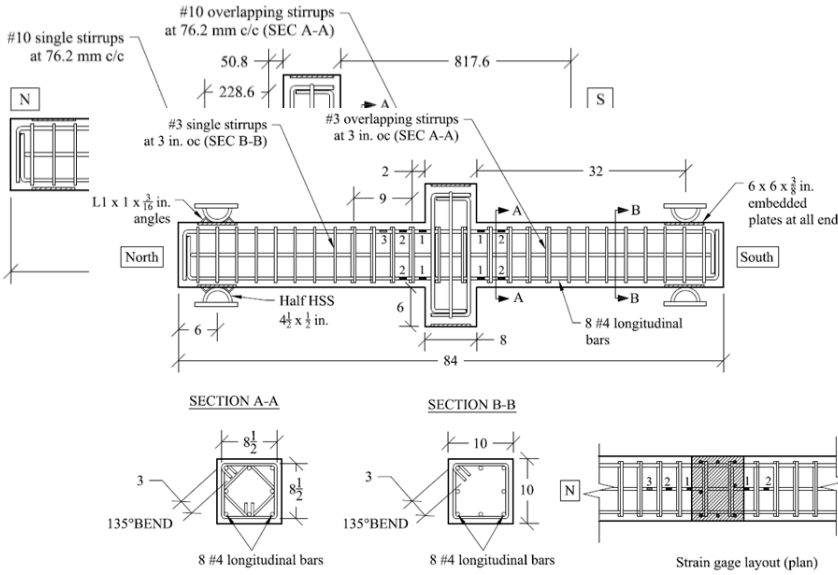

(a) (b)

Fig. 1 – (a) Experimental setup, and (b) Specimens' longitudinal and cross sections [Units in mm].

The target concrete compressive strength of all the specimens was f'_c = 82.7 MPa (12 ksi). The HSC cementitious materials included Type II Portland cement and silica fume. To increase concrete strength, the maximum coarse aggregate size was 9.5 mm (3/8 in.) and the water-to-cementitious material ratio w/cm was 0.33 [11]. Specimens were tested from seven to eight weeks after concrete casting, and in all cases f'_c exceeded the target strength at 28 days, as seen in Table 1. For HSFRC specimens, hooked steel fibers were added with a length-to-diameter aspect ratio of 60, and a fiber length of 33 mm (0.022 in.). The inclusion of steel fibers increased the compressive strength of HSFRC components about 9% with respect to that of HSC specimens S3 and S4. The compressive strength of HSCfy60 specimens (S1 and S2) was larger because the aggregates did not have the appropriate moisture content.

The specimens were reinforced with eight 12.7 mm (½ in.) diameter longitudinal rebars (Fig. 1b), resulting in a longitudinal reinforcement ratio $\rho_l = A_s/A_g =$ 1.6%, where A_s is the longitudinal reinforcement area, and A_g is the gross cross-sectional area. The transverse reinforcement consisted of 9.5 mm (3/8 in.) diameter stirrups spaced at each 7.6 mm (3 in.). The first six specimens had overlapping stirrups in the central section of the specimen, where plasticity is expected to occur (Fig. 1b). The effective depth of the section was d = 219.1 mm (8.63 in.), rendering a shear span-to-effective depth ratio $a/d = 3.7$. The first two components used conventional A615 Gr 420 (60) steel for both longitudinal and transverse reinforcement. The longitudinal A615 Gr 420 (60) rebars had a yield strength f_y = 450 MPa (65 ksi), an ultimate strength f_u = 715.0 MPa (103.8 ksi), and a 15% elongation in 203 mm (8 in.). Specimens 3 to 8 used ASTM A1035-11 Gr 690 (100) steel for longitudinal rebars and stirrups. The longitudinal rebars reported f_y = 924.0 MPa (134.0 ksi), f_u = 1,200.0 MPa (174.0 ksi), and a 9.5% elongation in 203 mm (8 in.) [2].

The specimens' confinement reinforcement ratio ($A_{sh}/s.b_c$) is presented in Table 1, where A_{sh} is the total cross-sectional area of transverse reinforcement, within spacing s, and perpendicular to the cross-sectional dimension of member core b_c. The minimum confinement reinforcement ratio, according to was ACI 318-14 Section 18.7.5.4 [12]:

$$\frac{A_{sh}}{sb_c} \geq 0.3\left(\frac{A_g}{A_{ch}} - 1\right)\frac{f'_c}{f_y} \quad (1)$$

where A_{ch} is the cross-sectional area measured to the outside edges of transverse reinforcement. According to Table 1, the confinement reinforcement in specimens 1, 2, 7, and 8 is smaller than that recommended by ACI 318-14, and acceptable for specimens 3-6, although it should be noted that Eqn. 1 does not consider the presence of steel fibers. Moreover, not complying with Eqn. 1 does not necessarily compromise the required component's shear capacity. According to ACI 318–14 Section 22.5, the shear capacity of the tested specimens was from three to five times larger than the ultimate shear load applied during the experiments.

Table 1 – HSC and HSFRC experimental tests

No.	Case * †	$f'_{c,test}$, MPa (ksi) at test day	Nominal f_y, MPa (ksi)	Fibers (% by vol)	$A_{sh}/s.b_c$	$A_{sh}/s.b_c$ (ACI 318)
S1	HSCfy60-M	108.9 (15.8)	413.7 (60)	-	0.0148	0.025
S2	HSCfy60-C	131.0 (19.0)	413.7 (60)	-	0.0148	0.031
S3	HSCfy100-M	99.3 (14.4)	689 (100)	-	0.0148	0.012
S4	HSCfy100C	97.9 (14.2)	689 (100)	-	0.0148	0.012
S5	HSFRC-M	106.9 (15.5)	689 (100)	1.0	0.0148	0.013
S6	HSFRC-C1	105.5 (15.3)	689 (100)	1.0	0.0148	0.013
S7	HSFRC-C2	117.9 (17.1)	689 (100)	1.0	0.0087	0.014
S8	HSFRC-C3	105.5 (15.3)	689 (100)	0.5	0.0087	0.013
* The target design f'_c for all specimens is 82.7 MPa (12 ksi) † Monotonic (M) and cyclic tests (C)						

2.2 Calibration of Backbone Curves from Experimental Monotonic Loading Tests

The experimental tests presented in these sections were used to calibrate a concentrated plasticity model, which was later used for numerical simulations. As shown in Fig. 2, these models can be applied because the spread of plasticity is not significant. For example, the cracks and spallation presented in Fig. 2a show that plasticity in specimen HSCfy60-M (S1) approximately extended 254 mm (10 in.) from the face of the stub, and failure was caused by fracture of one of the bottom longitudinal rebars. Specimen HSCfy100-M (S3) exhibited spallation at a drift of 2.5%, whereas HSFRC-M (S5) did not show spallation (Fig. 2b). In specimens HSCfy100-M and HSFRC-M the spread of plasticity was reduced, and the components failed due to a large flexural crack at the face of the stub that caused simultaneous fracture of the three longitudinal rebars. The addition of fibers did not increase the plastic length of the HSC with UHSS specimen.

Specimens HSCfy60-M, HSCfy100-M, and HSFRC-M were tested under monotonic loading protocols (Fig. 4). The two HSC specimens showed spallation, whereas the HSFRC specimen kept the concrete cover until failure. Spallation occurred in the HSCfy60 specimen at a total drift $\theta_T = 3.3\%$, resulting in a strength loss of about 20%. Because damage was concentrated on one side of the beam, the total drift reported in the study is the sum of the vertical stub drift (θ_v) and the rotational stub drift (θ_r):

$$\theta_T = \theta_v + \theta_r = \frac{\delta_{vs}}{a} + \emptyset_s . a \quad (2)$$

where δ_{vs} is the measured vertical drift at the stub edge, and $\emptyset_s$ is the stub rotation.

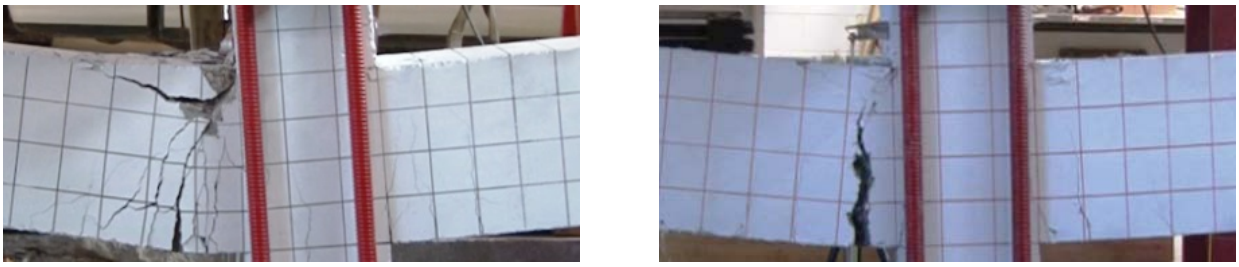

(a) (b)

Fig. 2 – Monotonic tests at rebar fracture (a) HSCfy60, S1; and (c) HSFRC, S5.

The force-drift relationships for the monotonic tests are presented in Fig. 3a, along with approximated backbone curves [2]. In the case of HSCfy60-M, the yield drift occurred at a vertical stub displacement $\delta_{y,vs}$ = 7.6 mm (0.3 in.), equivalent to a yield rotational drift θ_y = 0.009. The component reached its peak strength at about θ_c = 0.099, resulting in a beam-column ductility $\mu = \theta_c/\theta_y$ = 10.6, a relatively large value for a HSC component. Failure occurred after a flat post-capping slope was interrupted at a drift of about 16%, due to rebar fracture (Fig. 3a). The use of UHSS on specimen HSCfy100-M increased the specimen's peak strength by 60% with respect to that of HSCfy60-M specimen. However, after a small strength drop due to spallation, the maximum peak strength was reached at a drift ratio θ_c = 0.056 resulting in a ductility of only μ = 3.6. In addition, a steep negative slope followed the peak strength, causing a 75% strength drop due to fracture of the three beam-column bottom bars. To approximate this post-peak strength behavior, which includes two segments, a post-capping slope was adopted that reaches zero strength at about the same rotation as that of the experiment (θ_{pc} = 0.10). Specimen HSFRC-M was similar to HSCfy100-M, but the addition of a 1% by volume of steel fibers increased the initial stiffness, delayed cracking initiation and increased the peak strength by about 10% (Fig. 3a). Nevertheless, HSFRC-M nonlinear behavior did not improve because fibers prevented the spread of plasticity and did not increase the plastic length. Similar behavior has been reported for NSC beams with steel fibers [7].

The peak-oriented deteriorating hysteretic model developed by Ibarra et al. [13], and modified in OpenSees [14] by Haselton and Deierlein [15] was used to represent the components concentrated plasticity. Fig. 3b presents the model backbone curve, which includes an elastic stiffness, K_e; and a strain hardening stiffness $K_s = \alpha_s K_e$, where α_s is the strain-hardening ratio. This stiffness is capped at a maximum shear strength, F_c, or plastic moment capacity, M_c; and it is followed by a negative tangent stiffness $K_c = \alpha_c K_e$, where α_c is the post-capping stiffness. The chord rotation associated with the peak strength is θ_c, whereas the plastic deformation capacity is θ_p, and the post-capping deformation capacity at zero strength is θ_{pc}. The model may include a residual strength.

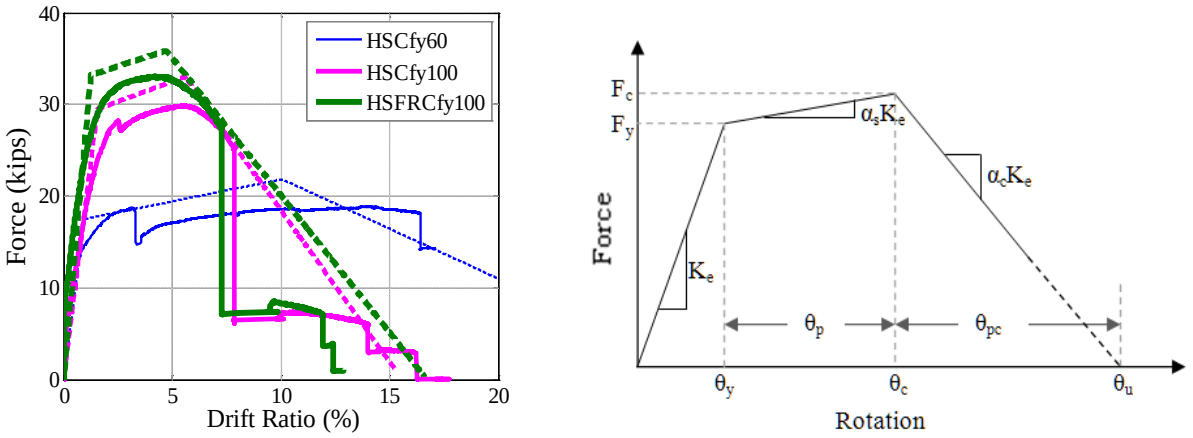

(a) (b)

Fig. 3. (a) Monotonic experimental curves, and proposed backbone curves, and (b) backbone curve Parameters for Ibarra-Krawinkler model (after Haselton and Deierlein [15]).

Table 2 summarizes backbone properties obtained from monotonic tests. Note that the computed stiffness slopes (α_s and α_c) represent material variations without geometric nonlinear effects because no axial loads were applied to the specimens. Also, although monotonic force-displacement curves for HSCfy100-M and HSFRC-M were less ductile than those of HSCfy60 specimens, they still exceeded ASCE 41-13 [16] force-deformation relationships.

Table 2 – Summary of backbone curve and deterioration parameters

Parameter	HSCfy60, S1 and S2	HSCfy100, S3 and S4	HSFRCfy100, S5 and S6	HSFRCfy100, S7	HSFRCfy100, S8
EI_{eff}	0.127EI	0.129EI	0.181EI	0.170EI	0.147EI
F_y, kN (kips)	77.8 (17.5)	131.2 (29.5)	147.7 (33.2)	(152.1) 34.2	(143.2) 32.2
F_c, kN (kips)	97.0 (21.8)	146.8 (33.0)	159.7 (35.9)	164.1 (36.9)	155.2 (34.9)
F_c/F_y	1.246	1.119	1.081	1.079	1.084
θ_y	0.0094	0.0156	0.0125	0.0138	0.015
θ_p	0.090	0.040	0.035	0.035	0.035
θ_c	0.0994	0.0556	0.0475	0.0488	0.05
θ_c/θ_y	10.57	3.56	3.80	3.54	3.33
θ_{pc}	0.20	0.10	0.12	0.10	0.10
α_s	0.026	0.046	0.029	0.031	0.036
α_c	-0.058	-0.175	-0.113	-0.148	-0.163
λ_s	250	50	35	80	60
λ_c	250	50	35	80	60

2.1 Calibration of Deterioration Parameters from Experimental Cyclic Loading Tests

Five specimens were tested under a cyclic loading protocol based on ACI-374 Committee [17], including three specimens identical to those tested under monotonic loading (Table 1). This displacement controlled loading protocol consisted of a series of pair of cycles that were monotonically increased as a function of the predicted yield displacement (Δ_y) until failure was reached. Because the yield displacement of HSCfy60-C (S2) is about half that of the specimens with UHSS, the number of cycles for the HSCfy60-C specimen at a given drift are about twice those of the rest of specimens. Fig. 4a presents HSCfy60 at 5% drift, showing that the plastic length extended within the first 10 in (254 mm) from the stub face, as in the monotonic test. Premature spalling was largely reduced in the cyclic loading test, possibly because small-displacement cycles led to early cracks that released energy from the concrete cover. Fig. 4b shows the specimen HSFRC-C1 (S6) at a drift of 5%, showing significantly less concrete spalling. The four specimens with UHSS subjected to cyclic loading failed due to a crack localized at the face of the stub. The phenomenon was more pronounced on the HSFRC elements because fibers prevented the spread of plasticity even further.

Fig. 5a compares the hysteretic response of HSCfy60 specimens under cyclic and monotonic response. Cumulative damage caused by the cyclic response reduces the specimen's strength and stiffness, particularly under high nonlinear excursions. The curve comparison shows the difficulties in estimating backbone curve parameters only from cyclic tests, as evidenced by the difference in the monotonic versus cyclic peak strength.

(a) (b)

Fig. 4 – Specimens under cyclic loading at the end of test (a) HSCfy60-S2, and (b) HSFRC-S6

The cyclic tests were used to calibrate two of the four cyclic deterioration modes of the Ibarra-Krawinkler model [13]: basic strength and post-capping strength deterioration modes, which translate the strain hardening and post-capping branch toward the origin, respectively. The amount of deterioration depends on the parameter β_i, which may be different for each cyclic deterioration mode. For instance, the strength in the i^{th} excursion ($f_{s,i}$) is deteriorated as:

$$f_{s,i} = (1 - \beta_{s,i}) f_{s,i-1} \tag{3}$$

where $\beta_{s,i}$ is the strength deterioration parameter in the i^{th} excursion. In general, β_i is obtained as

$$\beta_i = \left(\frac{E_i}{E_t - \sum_{j=1}^{i} E_j} \right)^c \tag{4}$$

where E_i is the hysteretic energy dissipated in excursion i, $\sum E_j$ is the hysteretic energy dissipated in previous positive and negative excursions, E_t is the total hysteretic energy dissipation capacity of component, and c is assumed equal to unity, implying a constant deterioration rate. In this study, the total energy hysteretic capacity was computed as a function of the yield stress and displacement: $E_t = \lambda_i F_y \delta_y$ [13]. The empirical parameters λ_i, associated to strength (λ_s) and capping strength (λ_c) cyclic deterioration modes, were calibrated from experimental tests. For the HSCfy60 component of Fig. 5a, strength and capping deterioration parameters $\lambda_s = \lambda_c = 250$ were obtained from the calibration in OpenSees [14]. These results correspond to slow cyclic deterioration rates usually associated to conforming NSC components [13,15].

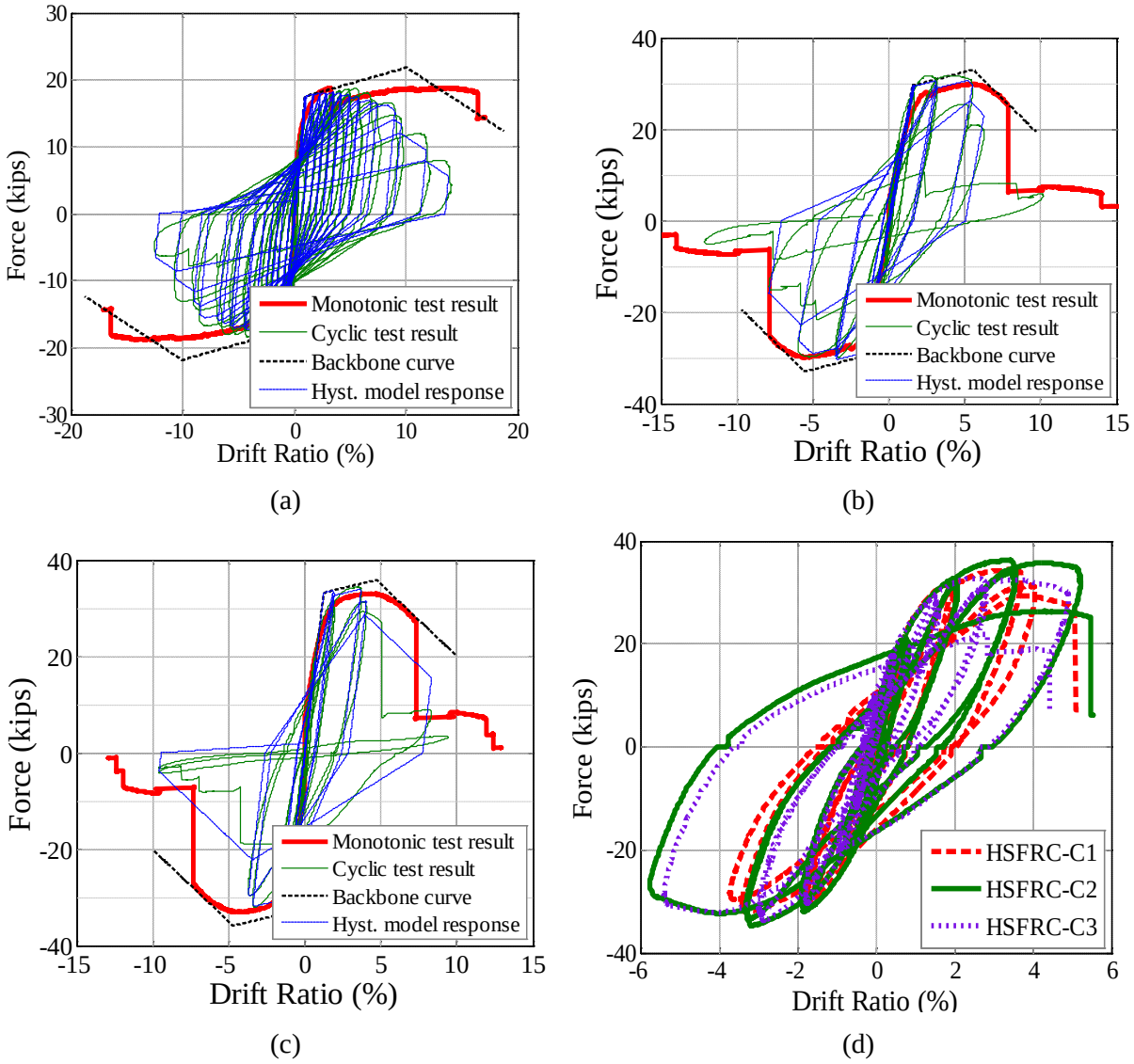

Fig. 5. Comparison of monotonic and cyclic experimental curves for (a) HSCfy60 (S1 and S2), (b) HSCfy100 (S3 and S4), and (c) HSFRC (S5 and S6). And (d) HSFRC components hysteretic behavior under cyclic loading.

Fig. 5b and 5c compare the experimental and numerical monotonic and cyclic responses of HSCfy100 and HSFRC specimens. In both cases, the monotonic curves had an ultimate strength 5-10% smaller than that of the cyclic curve, and the yield strength was adjusted prior to calibration of the deterioration parameters. For HSCfy100, the best fit of the hysteretic model and the experimental tests resulted when the cyclic deterioration parameters were $\lambda_s = \lambda_c = 50$, corresponding to fast cyclic deterioration [19,20]. As expected, the use of HSS reduced the inelastic energy dissipation capacity of the component.

For the HSFRC-C1 (S6) (Fig. 5c), the deterioration parameter values providing the best fit of the hysteretic curve are approximately $\lambda_s = \lambda_c = 35$. These parameters correspond to very fast cyclic deterioration, and indicate a poor inelastic energy dissipation capacity. HSFRC-C2 component had a better hysteretic behavior than HSFRC-C1 in terms of ductility and peak strength (Fig. 5d), rendering deterioration parameters $\lambda_s = \lambda_c = 80$, which are slightly better than the values obtained for HSCfy100-C1. This result is in agreement with Daniel and Loukili [15] study, in which they found that fibers do not significantly affect strength deterioration during cyclic loading. HSFRC-C2 included half of transverse reinforcement of HSFRC-C1, and 1% by volume of steel fibers.

HSFRC-C3 also had better behavior than HSFRC-C1 in terms of ductility, although it included half the transverse reinforcement and half the steel fibers by volume (i.e., 0.5%), see Table 1. The improvement in ductile behavior for specimens with less transverse reinforcement and/or steel fibers appear to indicate the HSFRC specimen S6 is over reinforced, an opposite conclusion from that drawn based on ACI 318-14 transverse reinforcement requirements. Note that previous studies have shown that ACI 318 [18] provisions provide a sufficient amount of transverse reinforcement to achieve drift ratios of at least 2% [29], but this amount of reinforcement may be conservative for low axial load level columns, especially if steel fibers are added, and contribute to the low spread of plasticity observed in HSFRC-C1 specimen.

3 APPLICATION OF HIGH STRENGTH MATERIALS TO SDOF SYSTEMS

SDOF systems were modeled to investigate the implications of the obtained experimental hysteretic responses on the seismic performance of HSC and HSFRC components.

3.1 SDOF System Characteristics

An elastic beam-column element with concentrated plasticity was used to evaluate the effect of HSC, HSS, and steel fibers on the nonlinear behavior of SDOF systems, using the above experimental test results. The evaluated SDOF systems had the same cross section and reinforcement of the experimental components, and approximately the same concrete and steel strength. Table 4 presents the basic characteristics of the four evaluated SDOF systems: i) NSCfy60, ii) HSCfy60, iii) HSCfy100, and iv) HSFRCfy100, based on S7 specimen. The first case is the reference case and assumes a NSC section that was not part of the experimental tests. Time history analyses were performed for these models considering no axial load, and an axial load P = 667 kN (150 kips). The period of vibration is affected by P-Δ effects, and variations in the elastic stiffness due to high strength materials. The percentage of critical damping was assumed as ξ = 5%.

Table 4. Nonlinear parameters of evaluated SDOF systems

Model	Period, T (s)		M_y , kN.m (kip.ft)		M_c/M_y	θ (rad)	θ_y (rad)	
	No P-Δ	P-Δ	With Axial load	No Axial load			With Axial load	No Axial load
NSCfy60 *	0.527	0.551	70.8 (52.2)	39.2 (28.9)	1.21	0.0849	0.011	0.0061
HSCfy60	0.513	0.535	90.0 (66.4)	42.3 (31.2)	1.25	0.0804	0.013	0.0063
HSCfy100	0.510	0.531	132.7 (97.9)	89.8 (66.2)	1.12	0.0794	0.020	0.0132
HSFRCfy100-C1	0.430	0.443	150.4 (110.9)	100.5 (74.1)	1.08	0.0565	0.016	0.0105
HSFRCfy100-C2	0.444	0.458	154.0 (113.6)	104.1 (76.8)	1.08	0.0603	0.017	0.0116
HSFRCfy100-C3	0.478	0.496	154.0 (108.2)	104.1 (71.5)	1.08	0.0699	0.019	0.0125
* f_c' is 34.5 MPa (5 ksi) for NSC, and 103.4 MPa (15 ksi) for HSC.								

The rotational springs were simulated based on the peak-oriented Ibarra-Krawinkler model, and included a softening post-capping stiffness in the backbone curve, as well as cyclic deterioration [13]. The nonlinear characteristics of the reference case, NSCfy60, were obtained from Haselton and Deierlein [15]. The model parameters for HSC and HSFRC components, summarized in Tables 4 and 5, were based on the monotonic and cyclic tests presented above. To account for the effect of axial load, the empirical equations proposed by Haselton and Deierlein [15] were used to get the parameter values with axial load. Once the parameter values

with no axial load were obtained from the tests, the results from the empirical equation were used to compute the reduction in the parameters due to the presence of axial load.

Table 5. Rotation capacities and cyclic deterioration parameter λ with and without axial load

Model	No Axial load			With Axial load		
	θ_p (rad)	θ_{pc} (rad)	λ	θ_p (rad)	θ_{pc} (rad)	λ
NSCfy60	0.080	0.10	200	0.046	0.070	111
HSCfy60	0.090	0.20	250	0.075	0.178	196
HSCfy100	0.040	0.10	50	0.033	0.089	40
HSFRCfy100-C1	0.035	0.12	35	0.029	0.107	26
HSFRCfy100-C2	0.035	0.10	80	0.029	0.089	57
HSFRCfy100-C3	0.035	0.10	60	0.029	0.089	43

3.2 Nonlinear Analyses of Models with no axial load, and with Axial Load and P-Δ Effects

Nonlinear dynamic analyses were performed in OpenSees for the SDOF systems subjected to a set of 22 far-field ground motions from FEMA-P695 [18]. The seismic intensity measure (IM) was the 5% damped spectral acceleration at the fundamental period of the system, $S_a/g\ (T_1)$. Thus the records were scaled based on $S_a/g\ (T_1)$, and for each ground motion, dynamic time-history analyses were conducted by increasing S_a/g values until the system response became unstable. These analyses, known as Incremental Dynamic Analyses (IDAs), can be represented with curves showing the relative intensity against an engineering demand parameter of interest. The IDA curves eventually approach a zero slope as S_a/g increases, and the restoring force in the backbone curve reaches zero during the loading path (Fig. 3b). The last point of the curves represents the system's "collapse capacity", $S_{a,c}/g$.

Fig. 6 shows median Sa/g - θ_{max} curves (i.e., intensity measure versus maximum drift) for the four evaluated systems, under no axial loading. The median curves are obtained from the IDAs of the 22 individual far-field ground motions. A comparison of NSCfy60 and HSCfy60 indicates that the use of HSC does not provide a significant benefit on the response of systems with no axial load. The use of UHSS on the HSCfy100 system improved the system behavior up to drifts of about 4% because the higher moment capacity results in a median elastic strength for the HSCfy100 component that is about twice that of HSCfy60. However, the system with UHSS reached collapse capacity at about the same spectral accelerations. Moreover, the HSCfy100 system exhibited failure at drift rotations of around 5-6% for most ground motions, which still is larger than the 0.03 rotation specified in ASCE 41-13, but about half the drift at which HSCfy60 system IDAS reached failure. Thus, the large increase in elastic capacity for components with UHSS is offset by their smaller θ_c value, steeper post-capping stiffness, and higher cyclic deterioration rates. The addition of fibers increased the HSCfy100 system's median collapse capacity, which was very similar to that of reference case NSCfy60. By assuming a lognormal distribution, the dispersion on collapse capacity can be expressed as the standard deviation of the log of the data $\beta = \sigma_{lnCC}$ [19]. In this example β = 0.62 and 0.40 for HSCfy60 and HSCfy100, respectively. The reduction of collapse capacity dispersion for cases with UHSS is a common characteristic of less ductile systems because the variations on ground motion frequency content are less relevant [19].

The benefits of using high strength materials, especially HSC, are influenced by the component's axial load level. If the components are subjected to an axial load P = 667 kN (150 kips), the normalized load is $P/f_c^{'}A_g = 0.10$ for systems with HSC, and $P/f_c^{'}A_g = 0.30$ for the NSCfy60 system. *P-Δ* effects can be related to the elastic stability coefficient, which is associated with a rotation of the original backbone curve. The stability coefficient is defined as [19]:

$$\theta = \frac{P}{k_e . h} \quad (5)$$

where h is the height of the system. For the evaluated models, stability coefficients were computed based on a specimen's length of 813 mm (32 in.). The coefficients fluctuate between $0.06 < \theta < 0.08$ due to the different period of the models (Table 4). These coefficients, based on dimensions of the tested specimens, would be relatively large for real buildings with fundamental periods around T = 0.5 s. because SDOF models do not account for the influence of parameters such as number of stories, distribution of vertical load, irregularities, and deflected shape, among others [19].

The median IDAs presented in Fig. 6b indicate that the HSFRC component renders the largest collapse capacity. The capacity reduction due to *P-Δ* effects is less pronounced in the HSFRC component because its larger stiffness and elastic strength lead to smaller drifts, whereas NSCfy60 collapse capacity is largely affected by *P-Δ* effects.

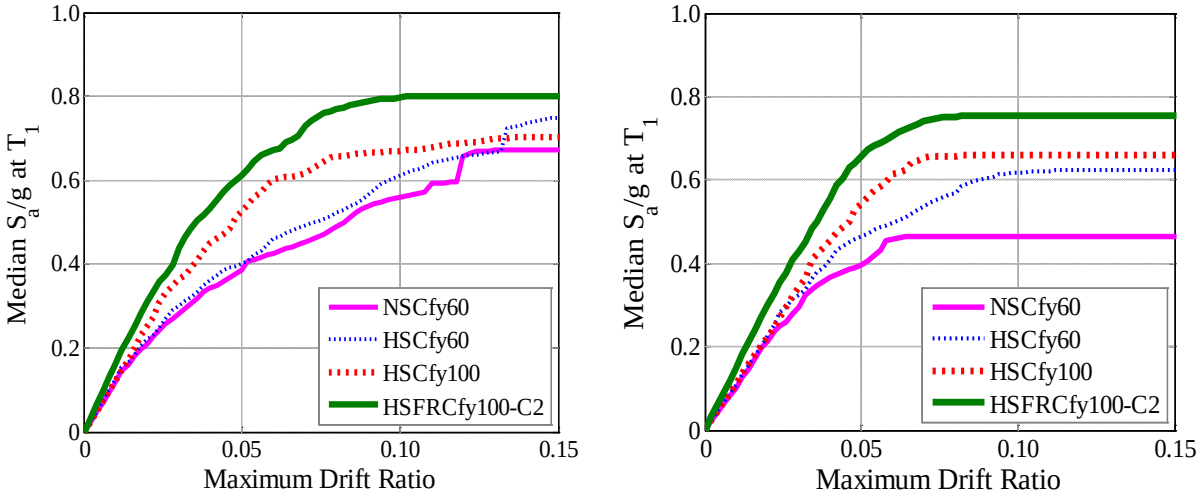

Fig. 6. Median Sa/g - θ_{max} IDA curves with no axial load, and for systems with axial load $P/f_c'A_g = 0.10$ (based on HSC capacity).

4 CONCLUSIONS

The study evaluates the seismic response of SDOF systems with high strength materials. First, experimental tests were performed on eight beam-column specimens under monotonic and cyclic loading. Then, nonlinear deteriorating parameters were calibrated using the experimental results, and the models were used to evaluate the seismic performance of SDOF systems with high strength materials up to the collapse limit state. The main findings of the research are as follows:

1. The drift at peak strength for HSC specimens with conventional steel (i.e., HSCfy60) was more than 80% larger than that recorded for HSC components with HSS (i.e., HSCfy100 and HSFRCfy100 specimens). Also, the cyclic deterioration rate, controlled by λ, is about five times slower for HSCfy60 specimens, as compared to HSFfy100 components.
2. Large spalling of concrete occurred at drifts of 3.3 and 2.5% drift ratio under monotonic loading for HSCfy60 and HSCfy100 components, respectively. Under cyclic loading the initial cycles create small cracks that release some of the energy in the component. Spalling was not detected on HSFRC subjected to monotonic or cyclic loading.

3. The addition of steel fibers did not increase the plastic capacity of the specimens for systems with the same confinement reinforcement (i.e., HSFRC-C1). The rotational capacity improved in specimens with smaller confinement reinforcement (e.g., HSFRC-C2).
4. The plastic length of HSCfy60 was larger than the effective depth "d". The use of UHSS on HSC (i.e., HSCfy100) reduced the plastic length of the component. The addition of fibers to HSC with UHSS specimens did not increase their plastic length.
5. The three specimens subjected to monotonic loading were used to calibrate the specimen's backbone curve parameters. The five cyclic experimental tests were used to evaluate cyclic deterioration of specimens with HSC and steel Grades 60 and 100 (i.e., HSCfy60 and HSCfy100), as well as for HSFRC .
6. The use of HSS reduces to half the drift at peak strength, and accelerates cyclic deterioration. The use of 0.5% by volume of steel fibers (instead of 1%) slightly reduces the deterioration rate.
7. The use of high strength materials on beam-column elements does not increase collapse capacity if no axial loads are applied. For systems with relatively large P-Δ effects, HSC and especially HSFRC components increase collapse capacity because of the smaller drifts under same seismic forces.

5 ACKNOWLEDGMENTS

The authors thank The University of Utah for providing funding for this study, Concrete Reinforcing Steel Institute (CRSI) for donating the steel rebars, and Maccaferri USA for supplying steel fibers used in the tests. Special thanks to M. Bryant, T. Nye, R. Uribe, R. Poudyal, M.J. Ameli, J. Parks, W. Xu, Y. Wang, C. Tucker, and S. Dangol, who collaborated during the fabrication and testing of the specimens.

6 REFERENCES

[1] Saatcioglu M, Razvi S. High-Strength Concrete Columns with Square Sections under Concentric Compression. Journal of Structural Engineering 1998; 124 (12): 1438-1447.

[2] Ibarra L and B. Bishaw (2016) "High Strength Fiber Reinforced Concrete Beam-Columns with High Strength Steel." ACI Structural Journal. Vol. 113, (01), pp. 147-156. January-February 2016.

[3] NEHRP Consultant Joint Venture. Use of High-Strength Reinforcement in Earthquake-Resistant Concrete Structures. NIST GCR 14-917-30; 2014.

[4] ACI Committee 544. Report on Fiber Reinforced Concrete (Reapproved 2009) ACI 544.1R-96. Farmington Hills, MI: American Concrete Institute; 2009.

[5] Campione G, La Mendola L, Mangiavillano ML. Steel fiber reinforced concrete corbels: Experimental behavior and shear strength prediction. ACI Structural Journal 2007; 104 (5): 570-579.

[6] Kimura H, Ueda T, Otake K, Kambayashi A. Structural Design of 80-Story RC High-Rise Building Using 200 MPa Ultra-High Strength Concrete. Journal of Advanced Concrete Technology 2007; 5 (2): 181-191.

[7] Tavallali H, Lepage A, Rautenberg JM, Pujol S. Concrete Beams Reinforced with HSS Subjected to Displacement Reversals. ACI Structural Journal 2014; 111 (5): 1037-1047.

[8] Daniel L, Loukili A. Behavior of High-Strength Fiber Reinforced Concrete Beams under Cyclic Loading. ACI Structural Journal 2002; 99 (3): 248-256.

[9] Ashour SA, Wafa FF. Flexural Behavior of High-Strength Fiber Reinforced Concrete Beams. ACI Structural Journal 1993; 90 (3): 279-287.

[10] Konstantinidis D, Kappos AJ. Seismic Evaluation of R/C Buildings Using High performance Materials. Advanced Materials for Construction of Bridges, Buildings, and Other Structures III 2003; 3 (12): 1-10.

[11] Bishaw B, L Ibarra (2012) "Optimization of High Strength Fiber Reinforced Concrete with Durability Characteristics for Seismic Applications." 15th World Conf. on Earthquake Eng. Lisbon, Portugal. Sept. 2012.

[12] ACI Committee 318. Building Code Requirements for Structural Concrete (ACI-318-11) and Commentary. Farmington Hills, MI: American Concrete Institute; 2011.

[13] Ibarra LF, Medina RA, Krawinkler H. Hysteretic Models that Incorporate Strength and Stiffness Deterioration. Earthquake Engineering and Structural Dynamics 2005; 34 (12): 1489–1511.

[14] McKenna F, Fenves G, Scott M. Open System for Earthquake Engineering Simulation, University of California, OpenSees. 2010; http://opensees.berkeley.edu/.

[15] Haselton CB, Deierlein GG. Assessing Seismic Collapse Safety of Modern Reinforced Concrete Frame Buildings, PEER Report 2007/08. Berkeley, CA: Pacific Earthquake Engineering Research Center; 2007.

[16] ASCE/SEI 41-13. Seismic Rehabilitation of Existing Buildings, ASCE standard. Reston, VA: American Society of Civil Engineers; 2013.

[17] ACI Committee 374. Guide for Testing Reinforced Concrete Structural Elements under Slowly Applied Simulated Seismic Loads, ACI 374.2R-13. Farmington Hills, MI: American Concrete Institute; 2013.

[18] Applied Technology Council. Quantification of Building Seismic Performance Factors - FEMA P695. Washington, DC: Federal Emergency Management Agency; 2009.

[19] Ibarra LF, Krawinkler H. Global collapse of frame structures under seismic excitations, PEER Report 2005/06. Berkeley, CA: Pacific Earthquake Engineering Research Center; 2005.